Enhanced Sensitivity of CO Photoacoustic Sensors Using Empirical Mode Decomposition Denoising Algorithm

Lei Li, Liping Tang, Fengtao Han, Shenghui Wang, Yang Gao, Yingying Qiao, *Member, IEEE*, and Chongxin Shan

***Abstract*—A CO sensor based on photoacoustic spectroscopy (PAS) with empirical mode decomposition (EMD) algorithm is investigated and demonstrated in this paper. In the PAS system, the complicated photo-thermal-acoustic conversion is a nonlinear and non-stationary process and contains various noise. In order to compensate the low signal-to-noise ratio (SNR), the EMD is introduced in the PAS system to deal with the photoacoustic signal. The experimental results show that a gain factor of ∼3.0 on the SNR is achieved and the sensor has an excellent linear response to the gas concentration. The minimum detection level (MDL) for CO detection is reduced to 1.14 ppm with a 300 ms integrated time at room temperature and atmospheric pressure.**

***Index Terms*—CO sensor, empirical mode decomposition algorithm, near-infrared light source, photoacoustic spectroscopy.**

I. Introduction

CARBON monoxide (CO), a highly toxic gas, is predominantly produced and released as a result of various incomplete combustion of hydrocarbons such as coal and oil [1]. When CO is inhaled, it can combine with hemoglobin which impedes the blood to carry oxygen to body tissues and vital organs, causing worldwide accidental deaths [2], [3]. The recommended exposure limit for CO established by National Institute for Occupational Safety and Health is 35 ppm as an 8-hour time-weighted average and 200 ppm as a ceiling [4]. Additionally, CO is one of the major global pollutants, which will react with hydroxyl (OH) to exacerbate global warming indirectly [5]. So that, there is an extensive demand to develop a ppm-level CO sensor for many applications.

Recently, photoacoustic spectroscopy (PAS) has become a popular optical method for trace gas detection due to its advantages of zero-background detection, high sensitivity, and fast response [6]. In view of the excellent performance of PAS, CO detection based on PAS has been widely studied in recent years. In 2019, Yufei Ma *et al.* reported a compact and sensitive mid-infrared (MIR) all-fiber quartz-enhanced photoacoustic spectroscopy (QEPAS) sensor for CO detection and obtained a minimum detection level (MDL) of 4.2 ppm [7]; Xukun Yin *et al.* stated a photoacoustic sensor system for CO detection using a 10 W fiber-amplified near-infrared (NIR) diode laser emitting at 1.56 μm, resulting in a ppb-level CO detection sensitivity in the same year [8]; In 2021, Davide Pinto *et al.* proposed a ppb-level QEPAS sensor for CO detection using a distributed feedback diode (DFB) quantum cascade laser emitting at 4.6 μm and obtained a MDL of 15 ppb [9]. In the above studies, the signal-to-noise ratio (SNR) of the sensors was improved by selecting mid-infrared light source, increasing the optical power and increasing the absorption optical path, so as to achieve the purpose of reducing the MDL. However, the flow noise, the ambient noise, background noise generated by window and cell wall absorption and electronic device noise are existed in the PAS system and seriously reduce the system performance. Using data processing algorithm to improve the SNR can improve the system performance without increasing the system complexity. Therefore, this method has important research significance for improving the performance of PAS trace gas detection.

So far, several denoising algorithms for PAS, such as moving average [10], Kalman filter [11] and wavelet transform [12], [13] have been developed to improve the SNR. These methods are suitable for dealing with linear signals, but the photoacoustic signal is nonlinear signal due to the gas absorption is a non-linear and nonstationary process with nonlinear absorption and various noise [14]. Hence, their performance will be severely limited in dealing with the photoacoustic signals. On the contrary, empirical mode decomposition (EMD) is a well-known denoising algorithm for nonstationary and nonlinear signal, which decomposes the signal according to the time scale characteristics of the data itself. It is regarded as an intuitive and adaptive signal processing method and holds the ability of making up for the inadequacies of other denoising algorithms [15]–[17]. In addition, the EMD combined with Savitxky-Golay (S-G) filter can retain waveform characteristics to the greatest extent and improve detection sensitivity. Hence, the EMD was adopted in this paper to improve the SNR and achieve high sensitivity of the PAS-based CO sensor.

Manuscript received February 13, 2022; revised April 11, 2022; accepted April 17, 2022. Date of publication April 22, 2022; date of current version May 3, 2022. This work was supported in part by the National Natural Science Foundation of China under Grants 62005247, 62027816 and 62105294, in part by the National Key Scientific Instrument and Equipment Development Project of China under Grant 6202780147, in part by the Henan Provincial Key Science and Technology Research Project under Grant 162102210018, and in part by Zhengzhou Collaborative Innovation Major Project under Grant 18XTZX12008. *(Corresponding author: Yingying Qiao.)*

The authors are with the School of Physics and Microelectronics, Zhengzhou University, Zhengzhou 450001, China (e-mail: lilei@zzu.edu.cn; zzutlp@163.com; hfengtao@yeah.net; shenghuiwang@foxmail.com; ieygao@zzu.edu.cn; qyy2019@zzu.edu.cn; cxshan@zzu.edu.cn).

Digital Object Identifier 10.1109/JPHOT.2022.3168966

In this work, a CO sensor based on PAS technique and the EMD is established. A near-infrared (NIR) distributed feedback (DFB) laser is employed as the excitation laser due to its stability and availability. Then, the optical power is boosted to ~300 mW by an erbium-doped optical fiber amplifier (EDFA). A differential photoacoustic cell (DPAC) is designed to suppress the flow noise and the ambient noise. During signal processing, the efficient EMD method combining with S-G filter and cross-correlation coefficient is employed to improve SNR and obtain high sensitivity.

II. Theory

A. The Photoacoustic Spectroscopy Principle

PAS is a zero-background optical detection method with ultra-high sensitivity. The photoacoustic signal is generated by non-radiative relaxation of periodically excited molecules, and it can be detected by microphone [18]–[20]. In the PAS system, the relationship between the absorption coefficient ($\alpha(v)$)and the absorbed light ($I(v)$) at a certain wavelength is described by Beer-Lambert Law [19],

$$I\left(v\right) = I_0\ \left(v\right)\left\{1 - \exp\left[-\alpha\left(v\right)l\right]\right\}, \tag{1}$$

where v is the wavenumber of the incident laser, $I_0(v)$ means the power of the incident light, $\alpha(v)$ is the absorption coefficient which is equal to the production of the total number density of molecules N_{tot}, concentration of the light-absorbing components C_m and the absorption cross section σ. For $\alpha(v)l \ll 1$, the relationship between the absorbed light $I(v)$ and absorption coefficient ($\alpha(v)$) can be regarded as linear. However, the complicated photo-thermal-acoustic conversion is a non-linear and non-stationary process and the photoacoustic signal will be contaminated by the thermoelastic noise [14], [21]. Hence, the photoacoustic signals show nonlinear and nonstationary characteristics.

Second harmonics wavelength-modulation spectroscopy (2*f*-WMS) is usually utilized to improve the SNR of the photoacoustic signal. A sinusoidal dither is used to modulate the light frequency. The detected electrical signal carries the information of CO absorption, which can be demodulated using a lock-in amplifier to obtain the 2*f* signal. The 2*f* signal derived from the photoacoustic signal is identified as the parameter related to the gas concentration by the following expression [19]:

$$S_{PA} = S_m\, C_{cell} P\alpha\cos\left(\varphi\right) \times H_2\left(v_0\right), \tag{2}$$

where, S_{PA} is the 2*f* signal detected by the microphone, S_m is the sensitivity of microphone, P is the incident laser power, C_{cell} is the cell constant, and α represents the gas absorption coefficient, φ is the phase difference between the 2*f* signal and the laser amplitude modulation, $H_2(v_0)$ is the 2*f* amplitude resulted from the Fourier cosine series expansion of the absorption profile at the absorption line-center (v_0).

It can be seen from (2) that the photoacoustic signal is proportional to the value of the cell constant ($C_{\rm cell}$). The $C_{\rm cell}$ of the resonator is affected by quality factor Q and the resonator dimensions. The $C_{\rm cell}$ of the first longitudinal mode for traditional H-type photoacoustic cell can be written as [22]:

$$\mathrm{C}_{cell} = -\frac{4(\gamma-1)QL_{eff}{}^2}{\pi^2 V_c c_s}, \tag{3}$$

where γ is the specific heat ratio, $L_{\rm eff}$ and $V_{\rm c}$ represent the effective cell length and the resonator volume, respectively. c_s, affected by temperature and type of gas in photoacoustic cell, is the sound velocity in the gas. Q is the quality factor, which represents the ratio of the energy stored by the system to the energy lost in a periodicity. Evidences show that decreasing the radius of the resonant cavity will increase thermal viscosity loss in the resonator, which will worsen the Q [22]. However, the $C_{\rm cell}$ is inversely proportional to the volume of the resonant cavity, as shown in the (3). Hence, in this paper, we choose the appropriate size of the photoacoustic cell to obtain the photoacoustic signal in the following experiments.

B. The Algorithm Principle

Photoacoustic signal is nonlinear and nonstationary because of the thermoelastic noise and nonlinear transition process [21], [23]. To reduce the impact of noise, EMD combining with the S-G filter and the cross-correlation coefficient will be introduced in this manuscript to process the photoacoustic signals. The EMD algorithm, a data-driven technique, decomposes the original signal into a group of adaptive intrinsic mode function (IMF) components based on the local time scale. The detailed decomposing process has been introduced in [14], [15].

For removing the noise from the original signal, the S-G filter is used to process each IMF component ($IMF_{\rm i}$) and residual component ($IMF_{\rm i}$/r). In fact, the key feature of the S-G filter is that it can keep the shape and width of the signal unchanged, so it is widely used in spectrum analysis [24]. The S-G algorithm processes the signal by polynomial least-square fitting inside a moving window. Then, the filtered components $DIMF_{\rm i}/Dr$ are reconstructed according to the cross-correlation coefficients ($C_{\rm i}/C_{\rm r}$) of $DIMF_{\rm i}/Dr$ and original signal. When the cross-correlation coefficient is larger than 0.4, the IMF is dominated by signal, otherwise it is dominated by noise. The noise-dominated component is removed directly. Finally, the reconstructed photoacoustic signal just includes the signal-dominated IMF components and the residual component. The above algorithm is named as de-noising algorithm based on EMD.

In PAS sensing system, a standard theoretical 2*f* signal of CO is simulated and taken as an example to verify the performance of the de-noising algorithm based on EMD. The infrared absorption spectrum of the CO molecule can be extracted from the HITRAN database [25]. In order to verify the denoising ability of the algorithm, the simulated 2*f* waveform is polluted by the gaussian noise. The wavelet denoising and the de-noising algorithm based on EMD are used to process the contaminated signals, respectively.

As show in Fig. 1, the black line represents the pure 2*f* signal of CO gas, the red line is the contaminated signal, the green line represents the filtered signal by wavelet transform and the blue line is denoised signal by the de-noising algorithm based on EMD. During the simulation, the random Gaussian white

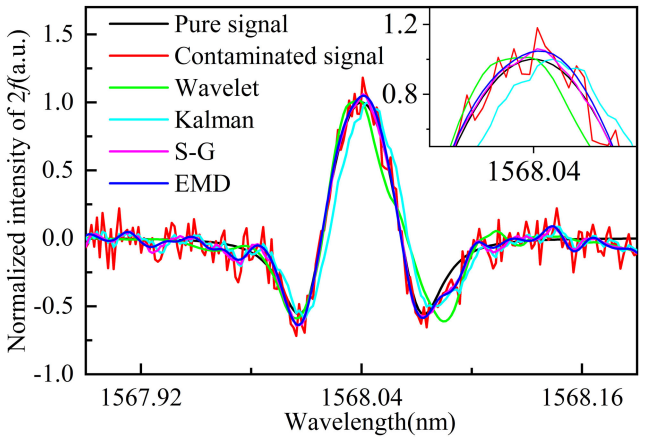

Fig. 1. Simulated second harmonics (2*f*) signal of CO at 1568.04 nm: the black line represents the theoretical pure 2*f* signal, the red line represents the contaminated 2*f* signal, the green line represents the filtered 2*f* signal by wavelet transform, the cyan line represents the filtered 2*f* signal by Kalman filter, the magenta line represents the filtered 2*f* signal by S-G filter, the blue line represents the denoised 2*f* signal by the de-noising algorithm based on EMD.

TABLE I
PERFORMANCE COMPARISON OF ALGORITHMS

	Wavelet	Kalman	S-G	EMD
SNR	11.0	9.6	16.0	16.1
SSIM	0.4	0.4	0.5	0.6

noise was added to the simulated 2*f* signal. Considering the randomness of the added noise, the SNR and the structural similarity (SSIM) were proposed as quantitative indexes to avoid the effects of subjective observation error. The SNR is calculated according to the following formula [26]:

$$SNR = 10 \times log_{10}\left(\frac{P_s}{P_n}\right), \tag{4}$$

where the P_s and P_n represent the power of the signal and noise, respectively. And SSIM value indicates the similarity between the original and denoised curves [27].

$$SSIM\ (x,y) = \frac{(2\mu_x\mu_y + c_1)(2\sigma_{xy} + c_2)}{({\mu_x}^2 + {\mu_y}^2 + c_1)({\sigma_x}^2 + {\sigma_y}^2 + c_2)}, \tag{5}$$

where the x is the original signal, y is the denoised signal, μ_x is the average of the x, μ_y is the average of the y, σ_{xy} is the covariance of the x and y, ${\sigma_x}^2$ and ${\sigma_y}^2$ denote the variances. c_1 and c_2, which close to zero, are regularization constants used to avoid instability for denominators.

As can be seen from the Table I, the SNR and SSIM of the signal dealt with the de-noising algorithm based on EMD are 16.1 and 0.6, the SNR and SSIM of the Wavelet denoised signal are 11.0 and 0.4, the SNR and SSIM of the Kalman filtered signal are 9.6 and 0.4. the SNR and SSIM of the S-G filtered signal are 16.1 and 0.5. Among them, the performance of the de-noising algorithm based on EMD is best, the denoised signal has the highest SNR and is most similar to the original signal. Hence, the de-noising algorithm based on EMD is more suitable to deal with the PAS signal.

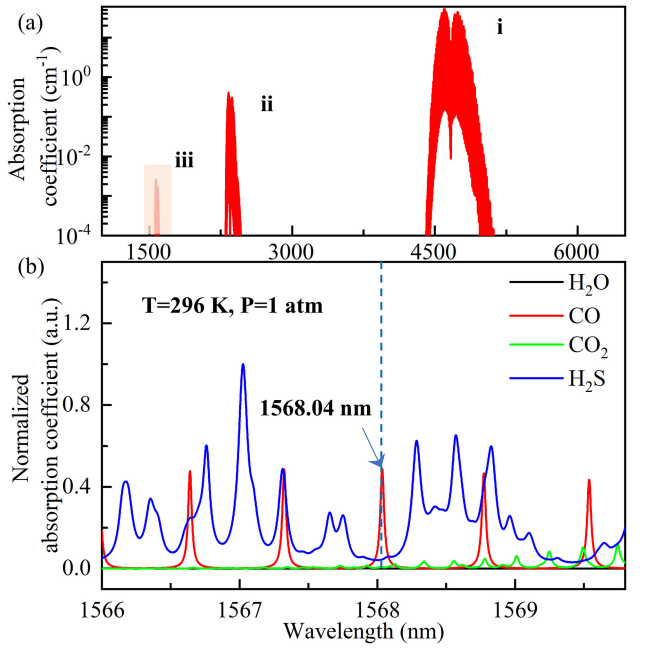

Fig. 2. (a) Three main CO absorption bands in the infrared region. i represents the fundamental band around 4.7 μm, ii represents the first obertone band located around 2.33 μm, and iii represents the second overtone band located at 1.56 μm. (b) The normalized absorption coefficients of several gases based on the HITRAN database.

III. EXPERIMENT

A. Near-infrared Absorption Line

The selection of absorption line of CO is according to HITRAN database. The CO absorption spectrum in the infrared region is plotted in Fig. 2(a). The line intensity of the second overtone band near 1.56 μm is weaker by several orders of magnitude than the fundamental band near 4.7 μm and the first overtone band near 2.33 μm. However, the second overtone band locates at optical fiber communication window, which means that the excitation laser and the optical components have been well developed and show more stable performance than other wavebands.

In order to achieve high-sensitive CO sensor, the absorption line with sufficient absorption strength and simultaneously avoiding interference from other gases will be chosen as the sensing wavelength. To select an interference-free CO absorption line, it is essential to carefully compare the absorption lines of some unavoidable active gas molecules in air. As shown in Fig. 2(b), the absorption line positions and normalized absorption coefficients of CO, H_2O, CO_2 and H_2S gas at 1 atm and 296 K are plotted. For the purpose of maximum interference preclusion, the absorption line located at 1568.04 nm will be chosen to detect trace CO concentration in the following experiments.

B. Experimental Set-Up

Fig. 3(a) illustrates the schematic of the PAS-based sensor for trace CO detection, which mainly consists of a DFB laser source

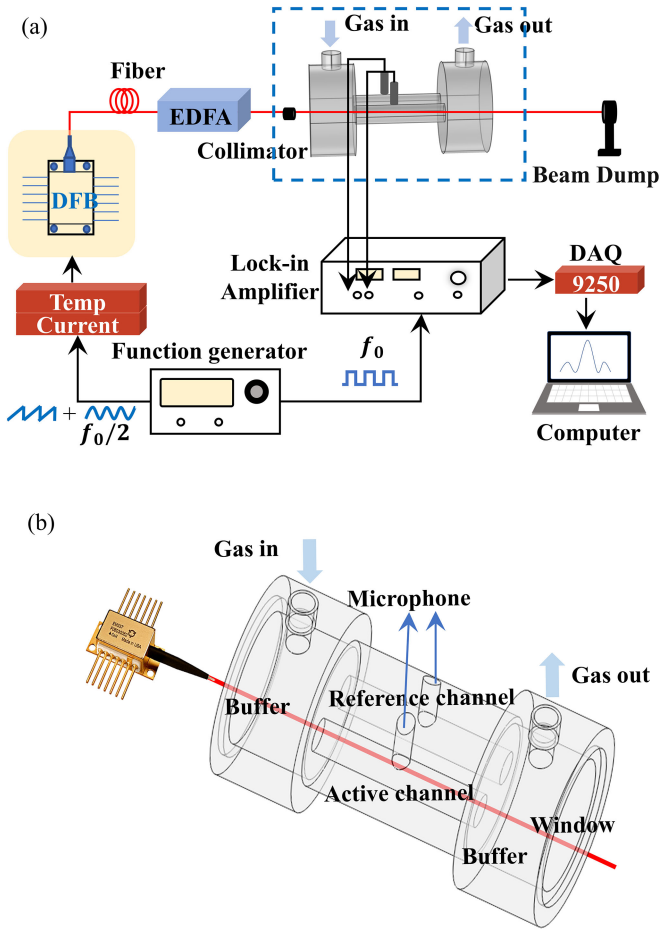

Fig. 3. (a) Schematic of the experimental setup. DAQ: data acquisition card; EDFA: erbium-doped fiber amplifier. (b) The structure of 3D-printed DPAC.

emitting at the wavelength of 1568.04 nm, a DPAC (as shown in Fig. 3(b)) in which the photoacoustic signal is produced, and a data acquisition and processing module.

During the experiments, a digital arbitrary waveform generator (Fluke 294) was used to generate a combinational signal consisting of a low frequency ramp wave and a high frequency sinusoidal dither. The ramp signal was used to slowly sweep the light wavelength from 1568.89 nm to 1568.19 nm. In order to obtain high sensitivity, 2*f*-WMS was applied to this system. So, the frequency of sinusoidal dither was set to one half of the DPAC resonance frequency. Then, the combinational signal was sent to a laser diode current source (ILX Lightwave LDX-3232) to drive and control the DFB laser (G&H E0067929). Meanwhile, a temperature controller (ILX Lightwave LDT-5525B) was employed to stabilize the operating temperature of DFB laser. The generated light beam was directed into an EDFA to boost the light power to ~300 mW. To pass through the DPAC with a resonator diameter of 6 mm without touching any surface, the output light from EDFA was collimated by an optical fiber collimator. Afterwards, the photoacoustic signal generated in the active channel of the DPAC and detected by an embedded microphone (BSWA MPA416 570074) with a sensitivity of 45.9 mV/Pa. At the same time, a same microphone was used

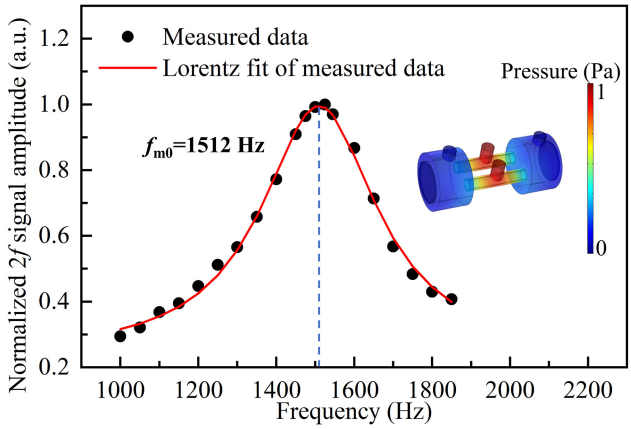

Fig. 4. The first-order longitudinal vibrational signal response curve of the DPAC obtained by experiment. Inset: first order resonance mode distribution. f_{m0}: measured first-order longitudinal resonance frequency.

to detect the signal that generated in the reference channel. Subsequently, the detected voltage signal was amplified by a pre-amplifier and then fed into the lock-in amplifier (Stanford Research Systems, USA, Model SR830) to demodulate in the 2*f* mode, whose reference signal was the synchronizing output signal of the sinusoidal dither. Finally, the voltage signal was acquired by a DAQ card (NI 9250) and sent into a computer to further process.

IV. Result and Discussion

A. Acoustic Resonance Analysis

The DPAC is constructed using a 3D stereolithography printer and the material employed for the 3D-printed DPAC is resin. It contains two 30 mm long cylindrical resonators with 3 mm radius. Both simulations and experiments are implemented to analyze the frequency response of the designed DPAC. As shown in the Fig. 4 , the peak of first-order longitudinal mode appears in the middle of the resonator. Hence the microphones are embedded in the middle of the resonator to detect the acoustic wave signal. During the experiments, the center wavelength of the DFB laser remained at the peak of the CO target absorption line. The 1% CO/N_2 gas mixture was fed into the gas sensor system. In order to accurately measure the DPAC frequency response at room temperature and pressure, the frequency of the sine signal was continuing tuned from 900 Hz to 1800 Hz. Because 2*f*-WMS was used, the modulation frequency should be equal to half the resonant frequency of the DPAC. The response curve shown in Fig. 4, which indicates that the DPAC has a resonance frequency around 3024 Hz ($2f_{m0}$) and it has a wide frequency response range. This wide frequency response can be attributed to the increase of bulk viscosity for the resonator with small radius [28].

B. Modulation Coefficient Optimization

In PAS system, the photoacoustic signal intensity can be optimized by adjusting the modulation current amplitude. In this experiment, the concentration of the used CO/N_2 gas mixture

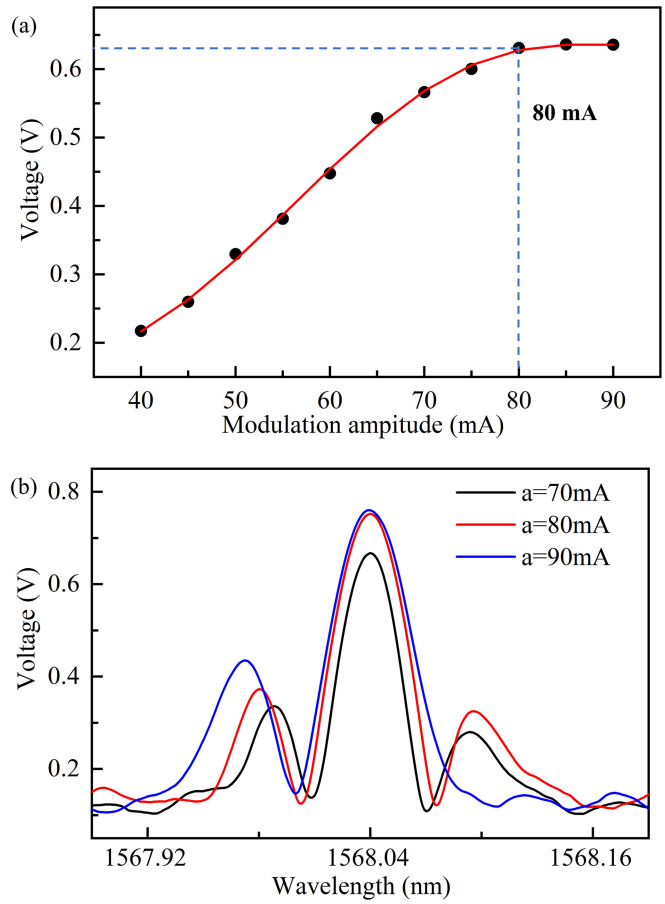

Fig. 5. (a) The 2*f* signal amplitude plotted as a function of different modulation current amplitude, (b) 2*f* signal waveform around 1568.04 nm with different modulation current amplitudes.

is 1%, and the scanning frequency of the ramp wave is 0.1 Hz at room temperature and pressure. The 2*f* signal amplitude as a function of different modulation current amplitude ranging from 40 mA to 90 mA is plotted in Fig. 5(a). It can be seen from Fig. 5(a) that the optimal signal amplitude is obtained when the modulation current amplitude is chosen to be 80 mA. Though the signal amplitude remains rising with the modulation current amplitude increasing larger than 80 mA, the 2*f* signal waveform is seriously distorted because of residual amplitude modulation [29], [30], as shown in Fig. 5(b). As a result, the modulation current amplitude is selected to be 80 mA in the following experiments.

C. Comparison of Sensor Performance With\Without EMD Filter

In order to verify the performance of the system and the effectiveness of the algorithm, the 2*f* signals for different CO concentrations were measured using the above system displayed in Fig. 2. Considering that the output wavelength of the laser needs to exactly remain to the central wavelength of the CO target absorption line, the initial driving temperature and current of the laser are set at 39.3 °C and 280 mA, respectively. A composite signal consisting of a 0.1 Hz pos-ramp wave and

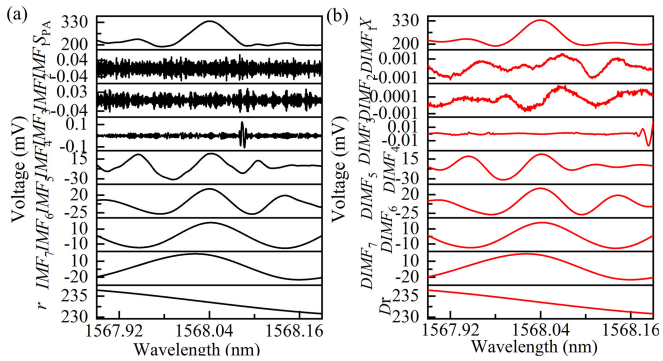

Fig. 6. (a) Original signal S_{PA} and its IMFs. (b) Reconstructed signal *X* and filtered IMFs by S-G filter.

TABLE II
THE CROSS-CORRELATION COEFFICIENTS OF THE DENOISED $DIMF_1$ AND THE ORIGINAL PHOTOACOUSTIC SIGNAL

C1	C2	C3	C4	C5	C6	C7	C8
0.15	-0.09	-0.007	0.55	0.73	0.72	0.59	0.06

a 1512 Hz sinusoidal dither is fed into the current controller to modulate the wavelength of the laser light. The CO/N_2 gas mixtures with different concentration are generated by a two-channel gas dilution system and pass through the DPAC at a flow rate of 200 sccm under the condition of room temperature and atmospheric pressure. The generated photoacoustic signal is detected by a microphone and then fed into the lock-in amplifier whose time constant is set to 300 ms to demodulate at 2*f* mode.

As shown in Fig. 6(a), S_{PA} is the original output signal of the lock-in amplifier, IMF_i represent IMF components obtained directly by EMD decomposition, *r* is the residual component. The original signal contains a variety of noise. The waveform of the original signal is distorted and the SNR value is low. According to the EMD principle, the original 2*f* signal is decomposed into seven IMF components and one residual component. Then, the S-G filter is applied to each IMF component and residual component. The filtered components are shown in the Fig. 6(b). It can be seen from the Fig. 6(b) that the high-frequency noise components have been largely filtered out, while the low-frequency component that dominated by the signal still retain the waveform and peak characteristics. Afterwards, the cross-correlation coefficients (C_i/C_r) between the filtered components and the original photoacoustic signal are calculated and the signal is reconstructed according to these parameters. When the cross-correlation coefficient is large than 0.4, the IMF is dominated by signal, otherwise it is dominated by noise. The noise-dominated IMF component is removed directly. Table II lists the cross-correlation coefficients.

As depicted in Fig. 7, the SNR of the reconstructed signal has been significantly improved. In Fig. 7(a), the original signal not only has high-frequency noise distribution (from IMF_1 to IMF_3), but also has noise and interference due to instrument noise, PAC wall and window absorption and the environmental influences. The noise data were continuously measured when the PAC was filled with pure N_2 and were plotted in the Fig. 7(b) and the

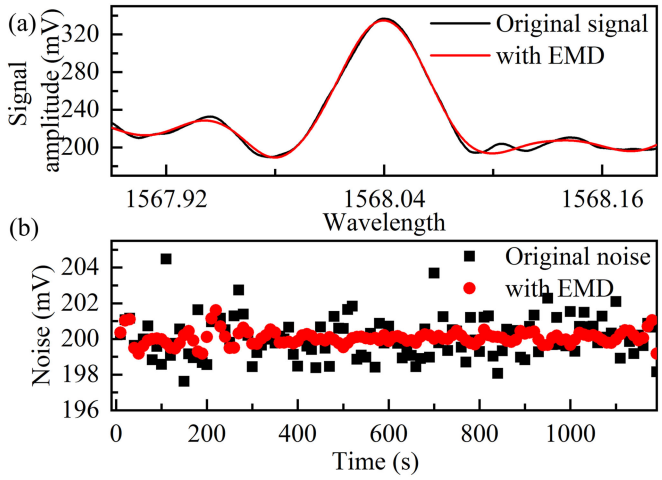

Fig. 7. (a) The 2*f* signal waveform of 1000 ppm CO with\without the de-noising algorithm based on EMD. (b) The noise fluctuations measured at the pure N_2 background.

TABLE III
COMPARISON OF SYSTEM PERFORMANCE PARAMETERS WITH\WITHOUT THE DE-NOISING ALGORITHM BASED ON EMD

Parameters	SNR	MDL (ppm)	R^2
Original data	295.4	3.39	0.985
with EMD	874.2	1.14	0.996

standard deviation (σ) of the noise data is defined as the system noise level. The calculated standard deviation (σ) of the detected voltage of the pure N_2 is 1.14 mV, and the SNR, calculated as the ratio of the peak value of the original photoacoustic signal ($\sim$336.7 mV) for 1000 ppm CO and the deviation (σ), is 295.4. When the de-noising algorithm based on EMD is used, the noise and interference are suppressed significantly. The peak value of the reconstructed signal is 332.2 mV and the standard deviation (σ) is decreased to 0.38 mV. The SNR value improves from 295.4 to 874.2, leading to an obvious improvement of SNR by a factor of $\sim$3.0. The MDL of the system can be given by a specific gas concentration and SNR, $c_{min} = c/SNR$.The MDL decreases from 3.39 ppm to 1.14 ppm. These parameters are listed in Table III.

Finally, gas samples with different concentrations were fed into the system to further study its performance. The relationship between the peak values of the 2*f* signals and the CO concentration is plotted in Fig. 8. As shown in Fig. 8, the signal amplitudes with the de-noising algorithm based on EMD exhibit the expected linear dependence on the CO concentration, and the linear correlation coefficient (R^2) improved to 0.996 from 0.985. It means that the detection repeatability and precision is improved. In addition, Table IV lists the comparison of the MDL of the PAS-based CO sensors. The sensor developed in this paper achieves high sensitivity under the premise of NIR laser light which can further expand its application prospect in practice.

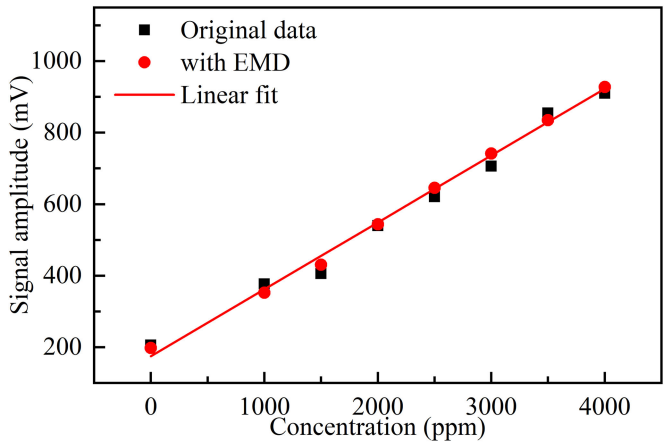

Fig. 8. Photoacoustic amplitude response vs. concentration before and after the de-noising algorithm based on EMD.

TABLE IV
PERFORMANCE COMPARISON OF THE DEVELOPED NIR PAS-BASED CO SENSOR

refs	light source	wavelength	power	sensitivity
31	TEDFL	1529.18 nm	500 mW	4 ppm
32	DFB	1570 nm	10W	342.7 ppb
33	DFB	1567.3 nm	10 mW	3.63 ppm
This paper	**DFB**	**1568.04 nm**	**300 mW**	**1.14 ppm**

V CONCLUSION

In conclusion, a PAS-based CO sensor based on a NIR excitation source and the de-noising algorithm based on EMD was demonstrated. A 1568.04 nm continuous wave DFB diode laser and an EDFA were applied to emit $\sim$300 mW light beam at the wavelength of target absorption line. However, to achieve ppm-level sensitivity, the power of the light beam at NIR region was usually needed to be boosted up to Watt-level. Therefore, this light power and various noise leads to low SNR which will seriously impact the sensitivity of the CO sensor. To solve the issue, the de-noising algorithm based on EMD was applied to reduce the effects of noises and the precision of measurement was improved by $\sim$3.0 times. With optimum design of the DPAC, optimal modulation frequency and modulation current amplitude, a sub-ppm level detection sensitivity was achieved. The results reported in this paper may provide a cost-effective route to photoacoustic sensors, thus push forward their future applications.

REFERENCES

[1] J. J. Rose *et al.*, "Carbon monoxide poisoning: Pathogenesis, management, and future directions of therapy," *Amer J. Respirat. Crit. Care Med.*, vol. 195, no. 5, pp. 596–606, 2017, doi: 10.1164/rccm.201606-1275CI.

[2] S. B. Jeon *et al.*, "Acute brain lesions on magnetic resonance imaging and delayed neurological sequelae in carbon monoxide poisoning," *JAMA Neurol.*, vol. 75, no. 4 pp. 436–443, 2018, doi: 10.1001/jamaneurol.2017.4618.

[3] C. C. Huang *et al.*, "Hyperbaric oxygen therapy is associated with lower short- and long-term mortality in patients with carbon monoxide poisoning," *Chest*, vol. 152, pp. 943–953, 2017, doi: 10.1016/j.chest.2017.03.049.

[4] Recommendations for occupational safety and health: Compendium of policy documents and statements, National Institute for Occupational Safety and Health (NIOSH), DHHS (NIOSH) Publication No. 92-10, 1992.

[5] M. A. Khalil and R. A. Rasmussen, "Carbon monoxide in the Earth's atmosphere: Increasing trend," *Science*, vol. 224, pp. 54–56, 1984, doi: 10.1126/science.224.4644.54.

[6] Z. Gong, K. Chen, Y. Yang, X. Zhou, W. Peng, and Q. Yu, "High-sensitivity fiber-optic acoustic sensor for photoacoustic spectroscopy-based traces gas detection," *Sensors Actuators, B Chem.*, vol. 247, pp. 290–295**,** 2017, doi: 10.1016/j.snb.2017.03.009.

[7] Y. Ma, Y. Tong, Y. He, X. Jin, and F. K. Tittel, "Compact and sensitive mid-infrared all-fiber quartz-enhanced photoacoustic spectroscopy sensor for carbon monoxide detection," *Opt. Exp.*, vol. 27, pp. 9302–9312, 2019, doi: 10.1364/OE.27.009302.

[8] X. Yin *et al.*, "Ppb-level photoacoustic sensor system for saturation-free CO detection of SF6 decomposition by use of a 10 w fiber-amplified near-infrared diode laser," *Sensors Actuators, B: Chem.*, vol. 282, pp. 567–573, 2019, doi: 10.1016/j.snb.2018.11.100.

[9] D. Pinto *et al.*, "Parts-per-billion detection of carbon monoxide: A comparison between quartz-enhanced photoacoustic and photothermal spectroscopy," *Photoacoustics*, vol. 22, 2021, Art. no. 100244, doi: 10.1016/j.pacs.2021.100244.

[10] B. Q. Fan *et al.*, "Lei, adaptive monostable stochastic resonance for processing UV absorption spectrum of nitric oxide," *Opt. Exp.*, vol. 28, pp. 9811–9822, 2020, doi: 10.1364/OE.384867.

[11] Y. Cao *et al.*, "Humidity enhanced N_2O photoacoustic sensor with a 4.53 μm quantum cascade laser and Kalman filter," *Photoacoustics*, vol. 24, 2021, Art. no. 100303, doi: 10.1016/j.pacs.2021.100303.

[12] L. Liu *et al.*, "Highly sensitive broadband differential infrared photoacoustic spectroscopy with wavelet denoising algorithm for trace gas detection," *Photoacoustics*, vol. 21, 2020, Art. no. 100228, doi: 10.1016/j.pacs.2020.100228.

[13] J. Zheng, Z. Tang, Y. He, and L. Guo, "Sensitive detection of weak absorption signals in photoacoustic spectroscopy by using derivative spectroscopy and wavelet transform," *J. Appl. Phys.*, vol. 103, 2008, Art. no. 093116, doi: 10.1081/ASR-120016391.

[14] Y. Meng *et al.*, "A modified empirical mode decomposition algorithm in TDLAS for gas detection," *IEEE Photon. J.*, vol. 6, no. 6, Dec. 2014, Art. no. 6803209, doi: 10.1109/JPHOT.2014.2368785.

[15] N. E. Huang *et al.*, "The empirical mode decomposition and the hilbert spectrum for nonlinear and non-stationary time series analysis," *Proc. Roy. Soc. London. Ser. A: Math. Phys. Eng. Sci.*, vol. 454, pp. 903–995, 1998, doi: 10.1098/rspa.1998.0193.

[16] A. O. Boudraa and J. C. Cexus, "EMD-based signal filtering," *IEEE Trans. Instrum. Meas.*, vol. 56, no. 6, pp. 2196–2202, Dec. 2007, doi: 10.1109/TIM.2007.907967.

[17] Z. Zhang, H. Xie, X. Tong, H. Zhang, Y. Liu, and B. Li, "Denoising for satellite laser altimetry full-waveform data based on EMD-Hurst analysis," *Int. J. Digit. Earth*, vol. 13, pp. 1212–1229, 2019, doi: 10.1080/17538947.2019.1698665.

[18] S. Weigl, F. Feldmeier, R. Bierl, and F. M. Matysik, "Photoacoustic detection of acetone in N2 and synthetic air using a high-power UV LED," *Sensors Actuators, B Chem.*, vol. 316, 2020, Art. no. 128109, doi: 10.1016/j.snb.2020.128109.

[19] Z. L. Wang, C. W. Tian, Q. Liu, J. Chang, Q. D. Zhang, and C. G. Zhu, "Wavelength modulation technique-based photoacoustic spectroscopy for multipoint gas sensing," *Appl. Opt.*, vol. 57, pp. 2909–2914, 2018, doi: 10.1364/AO.57.002909.

[20] K. Chen *et al.*, "Photoacoustic trace gas detection of ethylene in high-concentration methane background based on dual light sources and fiber-optic microphone," *Sensors Actuators B: Chem.*, vol. 310, 2020, Art. no. 127825, doi: 10.1016/j.snb.2020.127825.

[21] Z. Bozóki, A. Pogány, and G. Szabó, "Photoacoustic instruments for practical applications: Present, potentials, and future challenges," *Appl. Spectrosc. Rev.*, vol. 46, pp. 1–37, 2011, doi: 10.1080/05704928.2010.520178.

[22] M. R. Mohebbifar, "Optical measurement of gas vibrational-translational relaxation time with high accuracy by the laser photo-acoustic set-up," *Microchemical J.*, vol. 164, 2021, Art. no. 106040, doi: 10.1016/j.microc.2021.106040.

[23] S. Schilt and L. Thévenaz, "Wavelength modulation photoacoustic spectroscopy: Theoretical description and experimental results," *Infrared Phys. Techn.*, vol. 48, pp. 154–162, 2006, doi: 10.1016/j.infrared.2005.09.001.

[24] B. Zimmermann and A. Kohler, "Optimizing Savitzky–Golay parameters for improving spectral resolution and quantification in infrared spectroscopy," *Appl. Spectrosc.*, vol. 67, no. 8 pp. 892–902, 2013, doi: 10.1366/12-06723.

[25] I. E. Gordon *et al.*, "The HITRAN2016 molecular spectroscopic database," *J Quant. Spectrosc. Ra.*, vol. 203, pp. 3–69, 2017, doi: 10.1016/j.jqsrt.2017.06.038.

[26] C. H. Sherman and J. L. Butler, *Transducers and Arrays for Underwater Sound*. New York, NY, USA: Springer, 2007.

[27] R. Dosselmann and X. D. Yang, "A comprehensive assessment of the structural similarity index," *Signal Image Video Process.*, vol. 5, no. 1, pp. 81–91, 2011, doi: 10.1007/s11760-009-0144-1.

[28] R. Bauer, G. Stewart, W. Johnstone, E. Boyd, and M. Lengden, "3D-printed miniature gas cell for photoacoustic spectroscopy of trace gases," *Opt. Lett.*, vol. 39, pp. 4796–4799, 2014, doi: 10.1364/OL.39.004796.

[29] P. Patimisco *et al.*, "Purely wavelength- and amplitude-modulated quartz-enhanced photoacoustic spectroscopy," *Opt. Exp.*, vol. 24, pp. 25943–25954, 2016, doi: 10.1364/OE.24.025943.

[30] P. Patimisco *et al.*, "A quartz enhanced photo-acoustic gas sensor based on a custom tuning fork and a terahertz quantum cascade laser," *Analyst*, vol. 139, pp. 2079–2087, 2014, doi: 10.1039/C3AN01219K.

[31] J. Wang, W. Zhang, L. Liang, and Q. Yu, "Tunable fiber laser based photoacoustic spectrometer for multi-gas analysis," *Sensors Actuators, B Chem.*, vol. 160, pp. 1268–1272, 2011, doi: 10.1016/j.snb.2011.09.061.

[32] X. Yin *et al.*, "Near-infrared laser photoacoustic gas sensor for simultaneous detection of CO and H_2S," *Opt. Exp.*, vol. 29, pp. 34258–34268, 2021, doi: 10.1364/OE.441698.

[33] H. Cheng, X. Zhang, and C. Bian, *et al.*, "Photoacoustic spectroscopy: Trace CO detection by using 10 mW near-infrared laser and cantilever beam," *AIP Adv.*, vol. 10, no. 10 2020, Art. no. 1005122, doi: 10.1063/1.5134882.